MINISTRY OF EDUCATION AND TRAINING

VIETNAM ACADEMY OF SCIENCE AND TECHNOLOGY

GRADUATE UNIVERSITY SCIENCE AND TECHNOLOGY

TRAN THI THAI

THE SOURCES OF COSMIC-REIONIZATION AS SEEN BY MUSE/VLT

Major: Atomic and Nuclear Physics

Code: 9 44 01 06

SUMMARY OF PHYSICAL DOCTORAL THESIS

Ha noi 2024

The thesis has been done at: Graduate University of Science and Technology – Vietnam Academy of Science and Technology and Aix-Marseille University

Supervisor 1: Dr. Pham Tuan Anh

Supervisor 2: Dr. Roser Pello

Referee 1:

Referee 2:

Referee 3:

The thesis will be defensed in front of Jury committee at University level, Graduate University of Science and Technology – Vietnam Academy of Science and Technology

Time:

Looking for the thesis at:

- Library of Graduate University of Science and Technology
- National Library of Vietnam

Substantial summary

The success in operating astronomical instruments in recent years, such as Multi-Unit Spectroscopic Explorer (MUSE) at the Very Large Telescope (VLT), James Webb Space Telescope (JWST), etc., has driven research in the early Universe to become more dynamic than ever before. The ultimate goal of scientists working in this field is to study the sources of cosmic re-ionization and estimate their contribution to the re-ionization budget.

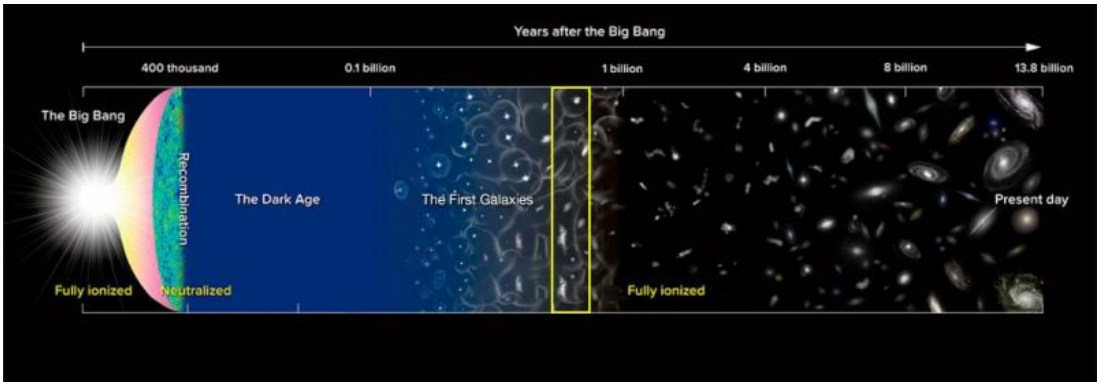

Figure 1: A brief history of the Universe from the Big Bang. The horizontal axis traces back time (top). The evolution phases of the Universe are shown from the time when the matter was fully ionized right after the Big Bang; after 380'000 years the recombination happened, at a redshift of 1100; after a few hundred million years the formation of the first structures (first stars, and galaxies) at the redshift of ~ 10, marked the end of the Dark Ages; the re-ionization was completed at redshift ~ 6. Credit: NAOJ

After the Big Bang, the temperature of the Universe was so hot that protons and electrons could not combine together to form the neutral hydrogen atoms. As the Universe expanded, its temperature cooled down, at ~ 3000K, it was cool enough for the formation of neutral hydrogen, marking the beginning of the Dark Ages. The Universe became transparent and the radiation from the Big Bang referred to as Cosmic Microwave Background could freely travel. Over time, the Universe continued to expand and cool creating conditions for the formation of the first structures such as stars and galaxies. The radiation from these structures will ionize the neutral hydrogen atoms surrounding them, marking the end of the Dark Ages and the beginning of the Epoch of re-ionization. This is considered a crucial stage in the evolution of the Universe.

Up to now, our understanding of the sources responsible for the reionization process remains unclear. It could be active galactic nuclei (AGN) with notable characteristics such as high brightness and high escape fraction of ionizing photons. However, the number of AGNs at redshift $z > 6$ that have been identified at the moment is not enough to maintain the epoch of re-ionization. Alternatively, it could be star-forming galaxies that provide ionizing photons thanks to young and massive stars. To address this question, the best approach is to study the contribution of these sources to the reionization process. In this thesis, I investigate the contribution of star-forming galaxies by studying the evolution of the Lyman-alpha Luminosity Function with redshift, providing valuable information regarding the galaxy density distribution within a given redshift range. Previous studies have predicted that faint, low-mass galaxies significantly contribute to the reionization process. To strengthen these theories, quantitative calculations and a more comprehensive picture

need to be developed. However, current observations in the field have not yet reached the faintest limit of luminosity, while observations based on gravitational lensing phenomena show improvement due to magnification. This thesis condenses on the galaxies emitting the Lyman alpha behind lensing clusters observed by MUSE/VLT.

The first chapter introduces the research topic, the current understanding of the first structures in the Universe, the ionization and recombination process. It also provides an overview of the spectral properties of star-forming galaxies, including characteristic features and methods to identify them from a given data cube. As we know, hydrogen is the most abundant element in the Universe, and electrons in the outer shell are easily excited to higher energy states in the interstellar medium so, Lyman alpha is the strongest line observable by ground-based optical astronomical instruments. At the moment, there are a number of galaxies have already detected at redshift $z > 6$, $\sim$ 10000 galaxies at redshift $z > 4$ from HST observations (Bouwens et al. 2015, Finkelstein et al. 2014), $\sim$ 18000 galaxies spectroscopically identified with Lyman alpha emission (HETDEX) at a redshift range of $z = 2.0 - 3.5$ (Zhang et al. 2021). The abundance of identified galaxies raises a question about their density in the early Universe and may estimate the contribution of star-forming galaxies to the cosmic reionization. This leads us to the definition of the Luminosity Function which tells us about number of galaxies that can be detected in a given luminosity range and a given cosmic co-moving volume. Studying the evolution of the Lyman alpha emitters luminosity function as a function of redshift is the most active branch at present to address the stated issue.

In Chapter 1, I also present an overview of recent results using observational Lyman alpha line data from astronomical observatories, combined with various approaches to probe the evolution of the Luminosity Function with redshift. However, information about the faint sources is limited as observations have not yet reached the necessary depth. The assumption of the slope value ($\alpha = -1.5, -2.0, -2.5$) of the Schechter function during fitting the Luminosity function points is often applied to recent research (Ouchi et al. 2008, Konno et al. 2018, etc). Scientific progress requires observational data to confirm theoretical models and estimate the galaxy density more accurately. Therefore, the thesis raises the issue of observing star-forming galaxies based on the gravitational lensing effect, a consequence of the relativistic Einstein theory, to obtain signals from Lyman alpha emitters in regions with a lower luminosity.

The second chapter briefly presents information about the Multi-Unit Spectroscopic Explorer (MUSE/VLT), its scientific goals, and the recent impressive results. The system allows the observation of multiple objects in a Field of View. The collected data contains information about the spatial location of the object, and its spectra in different wavelengths covering a range of 4750 Å to 9370 Å corresponding to the redshift of Lyman Alpha Emitters at a redshift range $2.9 < z < 6.7$.

In the third part of the chapter, I present the general features of 17 lensing clusters based on previous results and mass models of these clusters. Figure 2 is an example of spatial source distribution observed by MUSE. The different color circles correspond to the redshift of the sources. The main goal of MUSE is to investigate sources at a redshift of $z > 2.9$, therefore the number of sources at this redshift range is dominant compared to other ranges in the redshift distribution map. Figure 3 illustrates the procedure of inspection of the Lyman alpha emitter behind A2667 and determining its redshift value. To avoid subjective opinions during source inspection, there are three independent expert groups followed by a joint meeting to obtain the final conclusion about the redshift of the source and its confidence level. There are three different levels to assess the reliability of the redshift value of a source:

- $zconf = 1$: is the lowest level. At this level, the redshift of a source is identified based on a single weak emission line. We did not have 100% confidence to say that it is a Lyman alpha line, so this source was not used to study the Luminosity function of Lyman alpha emitters in the thesis. However, we discussed the effect of these sources on the uncertainty slope values of the Schechter function at different redshift ranges assuming they were included in the final data sample.

- $zconf = 2$. At this level, the redshift value of a source is identified based on several emission

lines. In some cases when the lines are not strong enough, but the observed image belongs to multiple systems, the confidence level of the redshift will be upgraded from $zconf = 1$ to $zconf = 2$.

- $zconf = 3$: the highest confidence level. The redshift of the source is identified based on several strong emission lines combined with absorption lines, the line profile that shows identified features, etc.

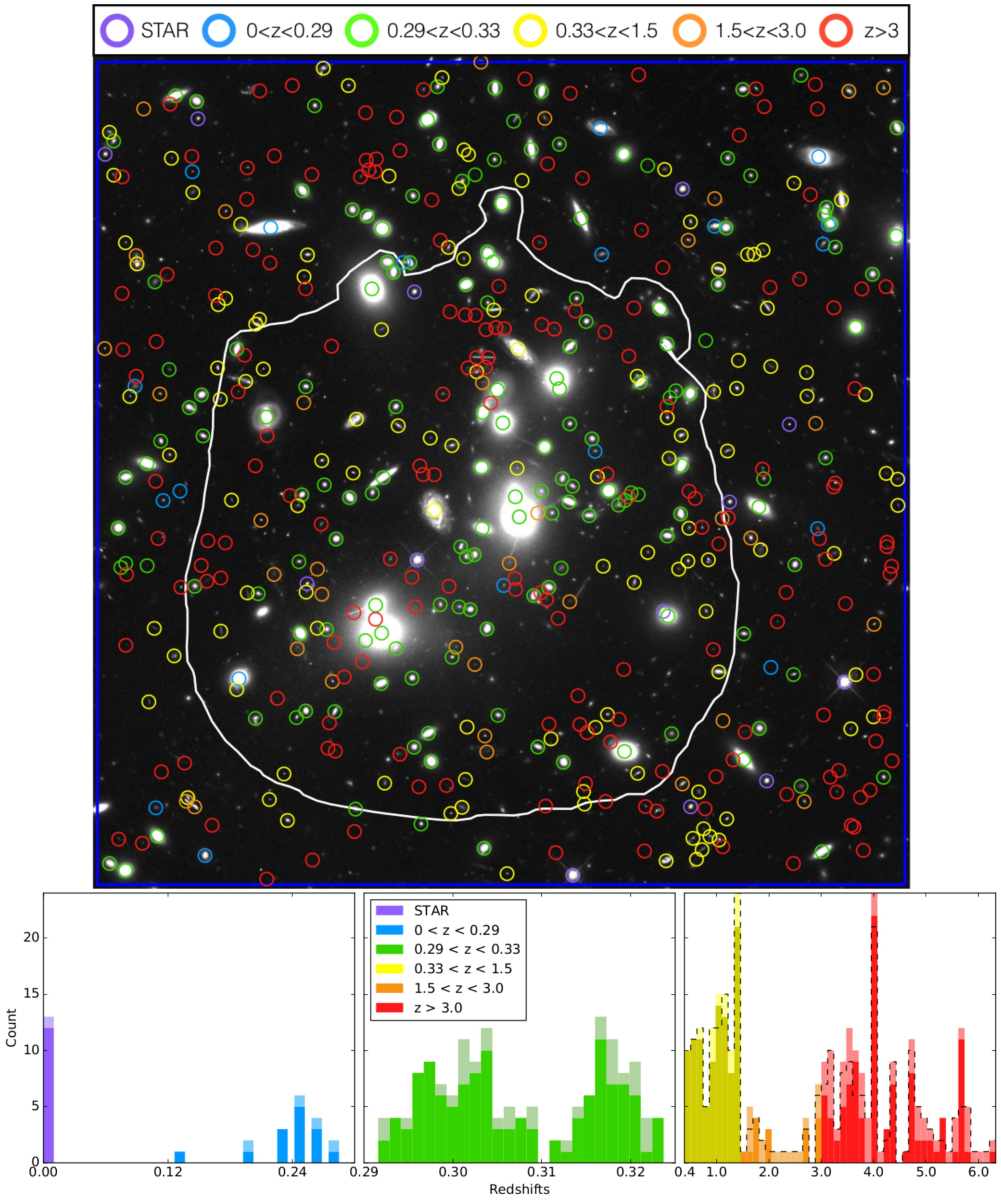

Figure 2: Upper panel: Spatial distribution of sources behind gravitational lensing cluster A2744 observed by MUSE and RGB HST. The lower panel is the redshift distribution of the sources. Credit: Mahler et al. 2018

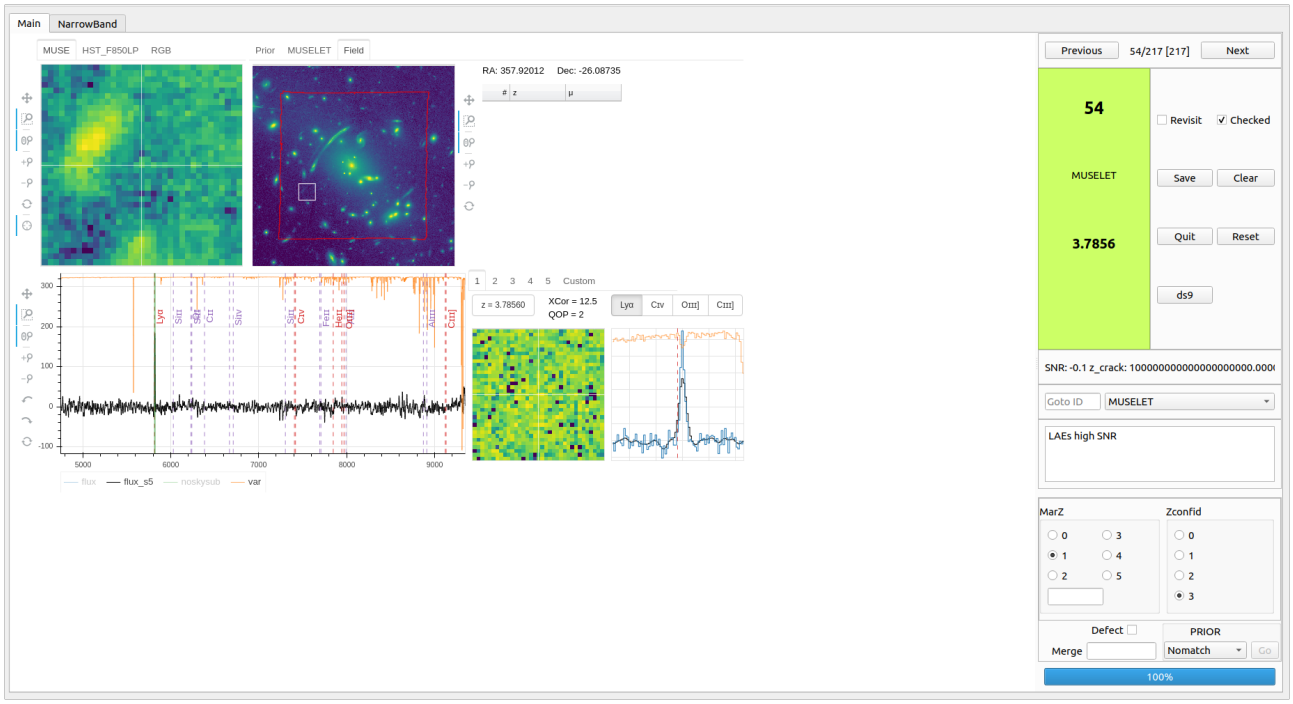

Figure 3: Interface of the source inspector software used to identified M54 source behind lensing cluster A2667 observed by MUSE and HST. The M54 is not well identified by HST observation (upper panel on the left). The upper panel on the right is A2667 MUSE FoV, the small red square denotes the region in which M54 is identified. Its spectra and zoomed-in profile are shown in the lower panel. The confidence level has been determined and recorded in the right column.

Because of the lensing effect, the signal from distant galaxies has been magnified, and the images have been distorted allowing be observation of multiple images of the same system. It is a complex analysis due to the requirement of projection back and forth between source and image plane. Aiming to limit computational redundancy and save time, in the context of my thesis, I selected only one representative image for each system based on criteria such as high SNR, reasonable magnification value, and the most isolated image compared to the others. The Chapter 2 concluded with general information about 600 Lyman alpha emitters behind 17 lensing clusters with redshift in the range $2.9 < z < 6.7$ (Table 1) covering four luminosity ranges $39 < \log L[\mathrm{erg/s}] < 43$ and compared with data from a previous study conducted by DLV 2019.
There are two notes during computing the Lyman alpha Emitters Luminosity Function:

- Flux of the sources. The data obtained from MUSE is stored as a data cube (2 spatial dimensions and 1 spectral dimension) so flux is estimated by spectral fitting method using a function proposed by Shibuya et al. 2014:

$$f(\lambda) = A \exp \frac{-(\lambda - \lambda_0)^2}{2(a(\lambda - \lambda_0) + d)^2} \tag{0.1}$$

where, A is the amplitude of the Lyman alpha spectra, a is asymmetric value of the Lyman alpha profile, d is FWHM. These parameters are optimized during fitting by applying the function form above to a subcube with a size of 5" × 5" × 12.5Å surrounding the source position. The mean value of FWHM and asymmetry were found to be 7Å and 0.2, respectively. The total flux value of the sources is taken from Claeyssens et al. 2022. In the case of faint sources in which the profile could not fit with the above equation, we use values obtained from the Source Extractor software which did not assume a parametric profile for the line. A comparison of flux values obtained from the two methods is presented in Figure 4 (left). The abscissa axis displays flux values measured from

SExtractor and the vertical axis is from spectral fitting, both in the unit of 10^{-18} [erg/s]. Linear fitting with a coefficient of 0.9 indicates the similarity between the two methods.

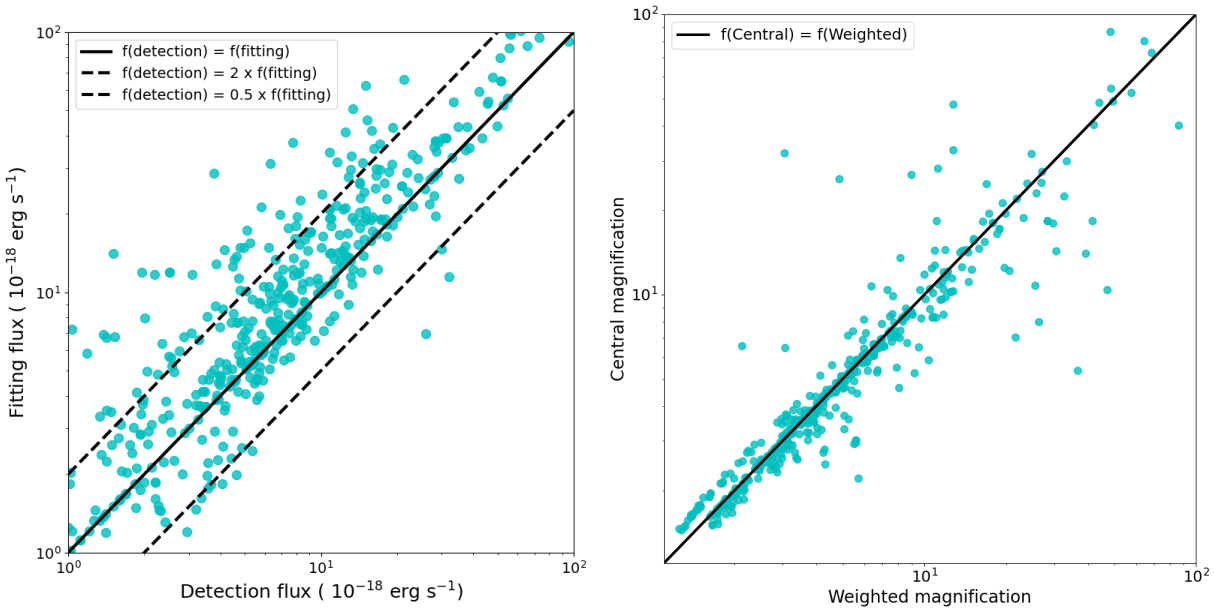

Figure 4: Left: Fluxes comparison obtained from two methods: Spectral fitting (y-axis) and SExtractor (x-axis). Right: Magnification comparison at central source (y-axis) and its weighted value (x-axis).

- Magnification value. Claeyssens et al. 2022 computed the magnification value of the source at its central position. In the case of an extended Lyman alpha image, the magnification varies across the image and the magnification value at one point of the image may not reflect the average integrated magnification value of the Lyman alpha emission in the complete image. To better account for extended sources, we prefer to use the weight value that has already accounted for this effect. The difference between these two values is illustrated in Figure 4 (right).

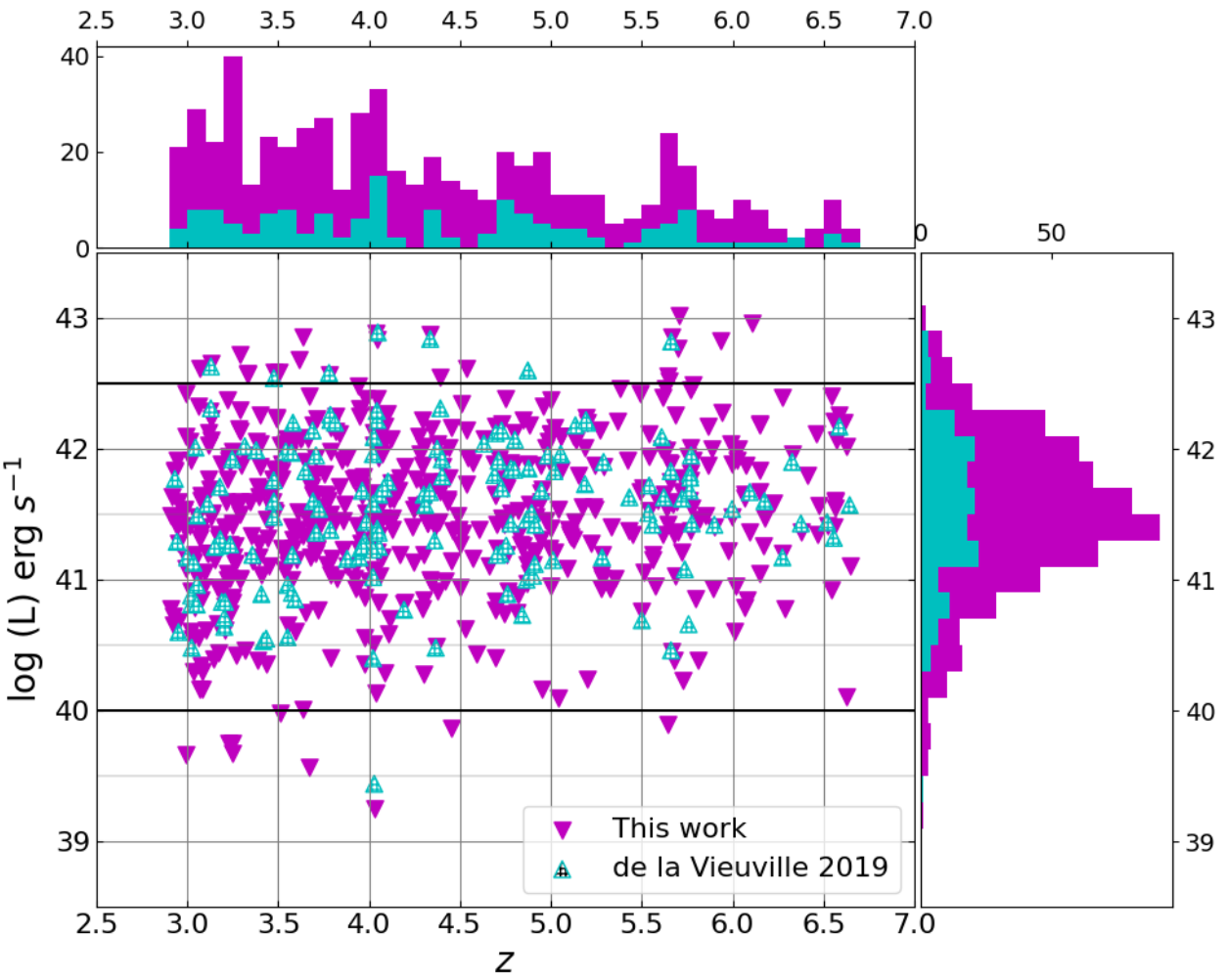

Figure 5: The central image displays the luminosity versus the redshift of the source. The Figure on the top is a redshift distribution. The Figure on the right is the luminosity distribution. The magenta color denotes values of 600 Lyman alpha Emitters used in the thesis compared to the data from DLV 2019 in cyan.

Compared to the previous data by DLV 2019 probing Lyman alpha emitters behind four lensing clusters, the number of sources in the current study is four times more. At the faintest level $\log L[\mathrm{ergs}^{-1}] \sim 40$, it indicates a significantly larger number of the sources in this work compared to the previous one. Therefore, the data used in the present work substantially improves the statistical data sample in this range. Figure 5 compares the current data with the previous data used in DLV 2019.

Table 1: General information of 17 lensing clusters observed by MUSE

Cluster	RA	DEC	z	Programme ID	Notes	Seeing value	MUSE depth (hrs)	N. LAEs
A2390	21:53:36.823	+17:41:43.59	0.228	094.A-0115		0.75	2	7
A2667	23:52:28.400	-26:05:08.00	0.233	094.A-0115		0.62	2	14
A2744	00:14:20.702	-30:24:00.63	0.308	094.A-0115, 095.A-0181	MACS, FF	0.61	3.5-7	128
A370	02:29:53.122	-01:34:56.14	0.375	094.A-0115, 096.A-0710	FF	0.66	1.5-8.5	41
AS1063	22:48:43.975	-44:31:51.16	0.348	60.A-9345, 095.A-0653	FF	1.02	3.9	20
BULLET	06:58:38.126	-55:57:25.87	0.296	094.A-0115		0.56	2	11
MACS0257	02:57:41.070	-22:09:17.70	0.322	099.A-0292, 0100.A-0249	MACS	0.52	8	24
MACS0329	03:29:41.568	-02:11:46.41	0.450	096.A-0105	MACS, CLASH	0.69	2.5	16
MACS0416N	04:16:09.144	-24:04:02.95	0.397	094.A-0115, 0100.A-0763	MACS, CLASH	0.53	17	45
MACS0416S	04:16:09.144	-24:04:02.95	0.397	094.A-0525	MACS, CLASH	0.65	11-15	32
MACS0451	04:51:54.647	+00:06:18.21	0.430	098.A-0502, 0104.A-0489	MACS	0.58	8	21
MACS0520	05:20:42.046	-13:28:47.58	0.336	098.A-0502, 0104.A-0489	MACS	0.57	8	19
MACS0940	09:40:53.698	+07:44:25.31	0.335	098.A-0502, 0101.A-0506	MACS	0.571	8	48
MACS1206	12:06:12.149	-08:48:03.37	0.438	095.A-0181, 097.A-0269	MACS, CLASH	0.521	4-9	49
MACS2214	22:14:57.292	-14:00:12.91	0.502	099.A-0292, 0101.A-0506	MACS	0.55	7	17
RXJ1347	13:47:30.617	-11:45:09.51	0.451	095.A-0525, 097.A-0909	MACS, CLASH	0.551	2-3	72
SMACS2031	20:31:53.256	-40:37:30.79	0.331	60.A-9100	MACS	0.79	10	20
SMACS2131	21:31:04.831	-40:19:20.92	0.442	0101.A-0506, 0102.A-0135	MACS	0.59	7	16
			Total:				**107-128**	**600**

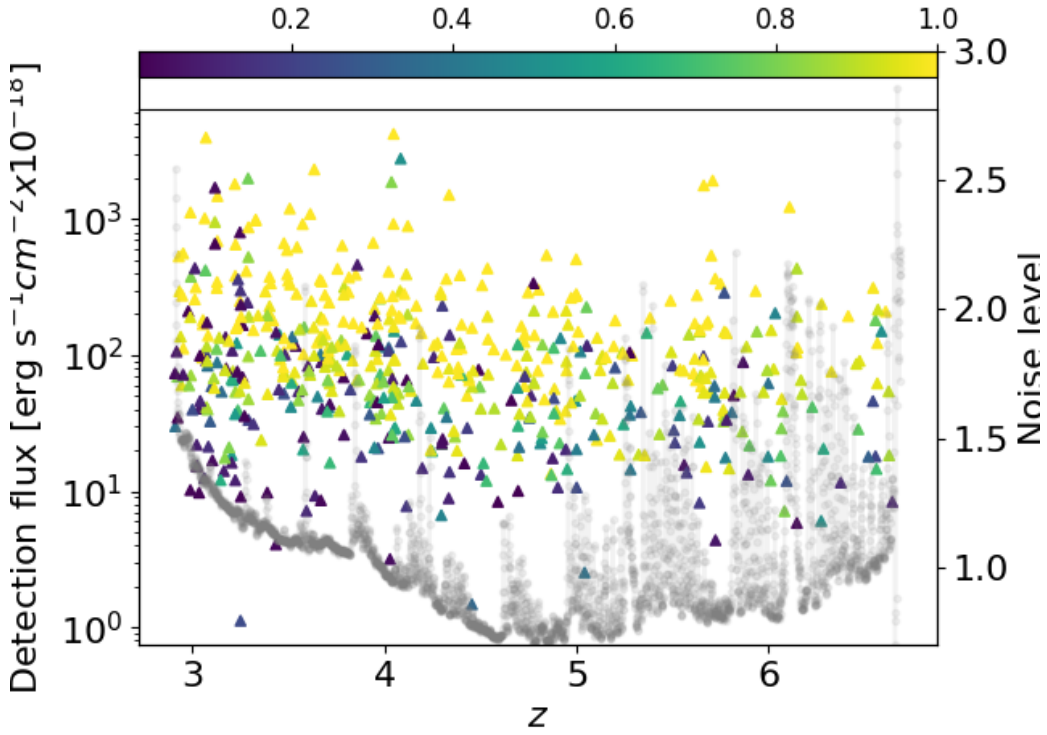

Figure 6: Detection flux and noise level in the sample versus redshift. The left axis displays the detected flux, the right axis gives the noise level (normalized), the lower horizontal axis is redshift and the upper one shows the completeness scale. The gray circles represent the evolution of noise level with redshift from the observation through the spectral dimension of the MUSE cube.

Chapter 3 describes the process of computing the $V_{\rm max}$ value for each source within our survey. In another way, $V_{\rm max}$ is the volume of a survey in which individual sources could be detected (Schmidt 1968). The contribution of the source to the density of galaxies is given by the reciprocal of this parameter. This thesis includes data collected in 18 regions (MACS0416 was observed in two regions); therefore, the $V_{\rm max}$ of individual sources must be calculated for all regions, including those where the source is absent. Working in the image plane to compute $V_{\rm max}$ value of individual sources may lead to an overestimate of this value. For this reason, the present work has been done in the source plane, based on the creation of 3D cube in the source plane for each source. The pipeline was initially developed by DLV 2019 to study the luminosity function of 128 Lyman alpha emitters behind only four lensing clusters. In this chapter, I summarize the main steps, with some new improvements that have been taken into account for the calculation procedure, and make a comparison of the obtained result on the volume of the survey to the previous work. It is worth mentioning that the present results indicate a total co-moving volume of approximately 50000 Mpc^3, which is three times larger than that in DLV 2019. However, this value is significantly smaller than the one found in the works using data observed in the blank fields, due to the constraints imposed by gravitational lensing effects, which reduce the effective total field of view.

Chapter 4 presents the main results of the thesis on the luminosity function of 600 Lyman alpha emitters in four redshift intervals. By definition, the luminosity function is the number of galaxies per unit of co-moving volume (number density), per luminosity interval. To compute the luminosity function, in addition to determining the $V_{\rm max}$ of a source as described above, one must account for the fact that not all sources in the data sample have a 100% probability of being detected. Hence, we need to correct for completeness, which gives the true probability of finding a source in the cube. The procedure was carried out for each source by reconstructing the profile of the galaxy in the image plane and randomly injecting this model into different places in the cube,

Cluster	Total co-moving volume [Mpc^3]
A2390	735
A2667	885
A2744	10500
A370	5350
AS1063	1970
BULLET	895
MACS0257	730
MACS0329	1225
MAC0416N	3420
MACS0416S	1670
MACS0451	1210
MACS0520	765
MACS0940	5760
MACS1206	2980
MACS2214	1100
RXJ1347	7920
SMACS2031	1675
SMACS2131	920
Total	49710

Table 2: Total co-moving volume of 17 gravitational lensing clusters in the present work within a redshift range of $2.9 < z < 6.7$.

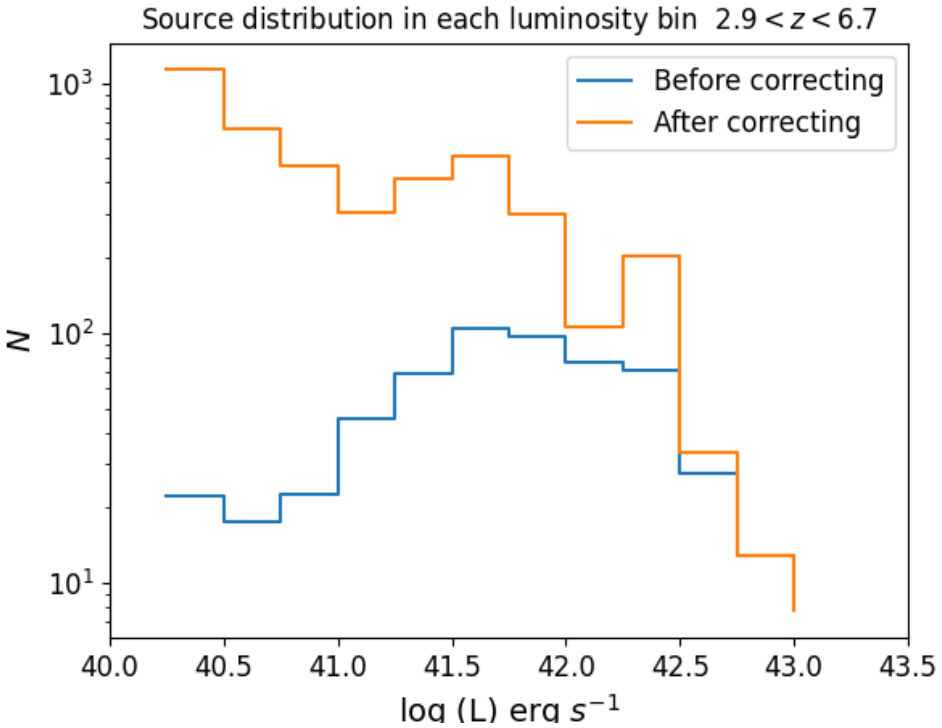

Figure 7: Source distribution in the redshift interval $2.9 < z < 6.7$ for a luminosity bin width of 0.25 in logarithmic scale. The blue and orange lines are the distribution before and after correcting for completeness.

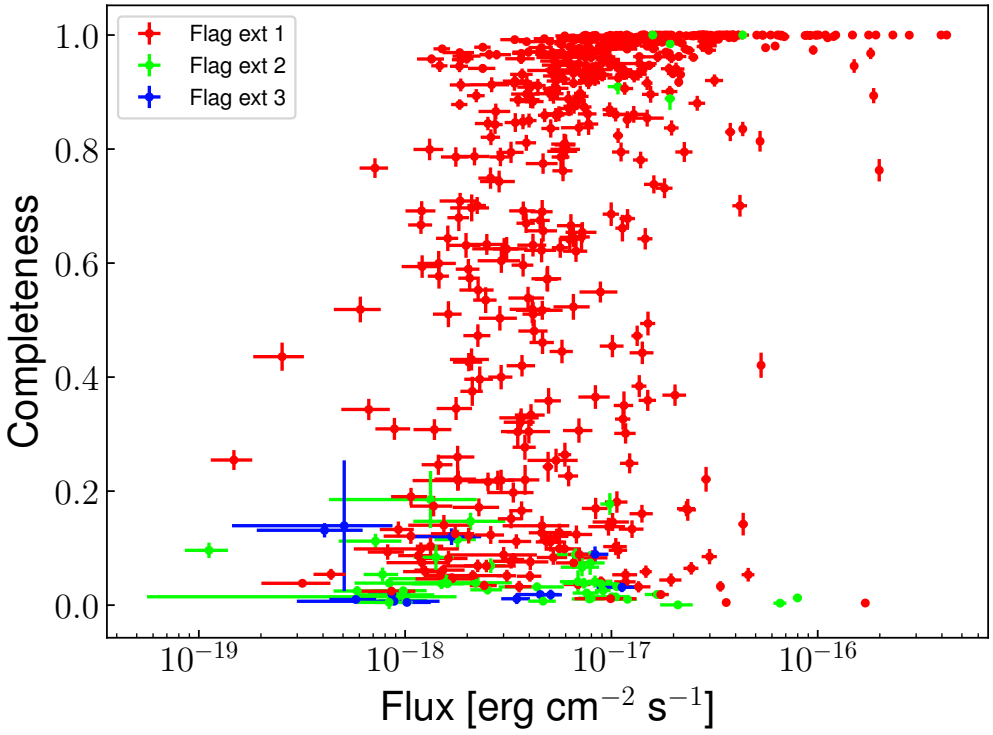

Figure 8: Completeness vs. detection flux of LAEs from the present sample. Different colors indicate the quality of extraction from SExtractor. Only sources in the unmasked regions of the detection layer are considered here.

to capture the real effect of the noise. The source is considered to be detected when the maximum deviation between the injected position and the detected position of the source is less than 0.8". The completeness is determined directly by the ratio between the number of successful detections, under the same conditions as the original extraction, and the number of objects injected. There are several differences between this work and that of DLV 2019 in consideration of completeness, as well as in the detailed discussion of selection effects.

- The impact of image size on the final result of completeness value has been discussed. The size has to be large enough to capture the noise in the source region of the slice where the Lyman alpha emission line reaches the peak. In the thesis, I increase the size from 30" × 30" to 80" × 80".

- With the goal of maximizing the number of sources used for the luminosity function computation and subsequent advancements, we have excluded sources with completeness values below 1%. Compared to the work by DLV 2019, this value was set at 10%. Using 1% completeness for source detected correction is normal as the recent study on Luminosity Function did not mention the threshold, they believed that the sources were real because it was confirmed by the lensing model.

- The detected flux, noise level, and completeness with respect to the redshift of individual sources are shown in Figure 6. The number of sources used for the Luminosity Function in the whole redshift interval, for different luminosity intervals, has been presented in Figure 7, before and after completeness correction. Figure 6 shows that most faint sources have an extremely low completeness value. However, when the correction of the completeness parameter is taken into account, the number of sources in these bins increases significantly. On the other hand, for sources allocated in the bright parts, the probability of detection is already high, so whether we apply the completeness correction or not does not markedly change the source distribution. In the luminosity range $42.25 < \log L\ [\mathrm{erg\ s^{-1}}] < 42.5$ of Figure 7, the appearance of a spike can be explained by the existence of low completeness sources distributed within the given luminosity range.

Table 3: The best-fit values of the Schechter function at different redshift intervals.

Redshift	$\Phi*$ [10^{-4}Mpc^{-3}]	$\log L*$[erg s^{-1}]	α
$2.9 < z < 6.7$	$7.41^{+2.70}_{-2.20}$	$42.85^{+0.10}_{-0.10}$	$-2.06^{+0.07}_{-0.05}$
$2.9 < z < 4.0$	$6.56^{+3.20}_{-2.40}$	$42.87^{+0.11}_{-0.1}$	$-2.00^{+0.07}_{-0.07}$
$4.0 < z < 5.0$	$4.06^{+2.70}_{-1.70}$	$42.97^{+0.13}_{-0.11}$	$-1.97^{+0.09}_{-0.08}$
$5.0 < z < 6.7$	$3.49^{+2.11}_{-1.50}$	$43.09^{+0.10}_{-0.08}$	$-2.28^{+0.12}_{-0.12}$

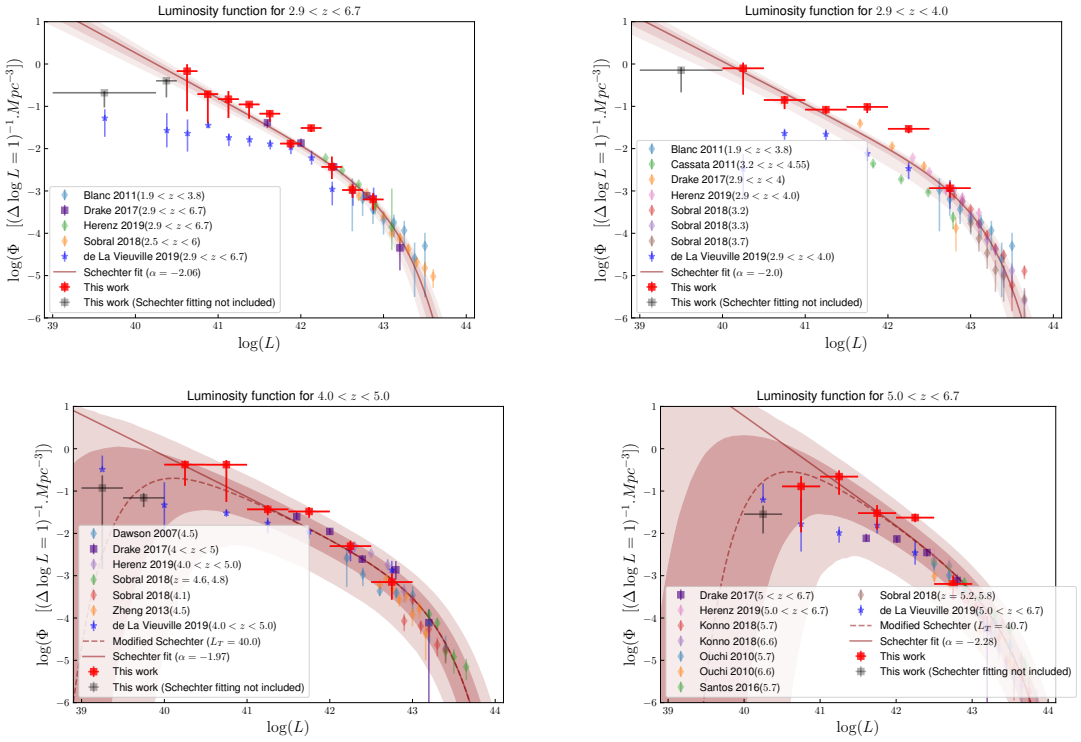

Figure 9: From left to right, top to bottom shows the luminosity function in different redshift intervals: $2.9 < z < 6.7$, $2.9 < z < 4.0$, $4.0 < z < 5.0$, and $5.0 < z < 6.7$. The red crosses represent the results of this work, while other colors in the bright end indicate data from the literature. The blue ones are results from (DLV 2019) used for comparison purposes. The solid brown reddish line is the best-fit Schechter function. The gray crosses obtained from the present work are not included in the fit. The reddish dashed lines correspond to the best fit with a Schechter function modified to take into account the turnover observed in the data points towards the faint end.

The luminosity function point within a given redshift bin and a given luminosity range follows the function below:

$$\Phi(L_i) = \frac{1}{\Delta \log L_i} \sum_j \frac{1}{C_j V_{\max,j}} \tag{0.2}$$

where $C_j, V_{\max,j}$ is the completeness and $V_{\max}$ of a given source, $\Delta \log L_i$ is the i^{th} luminosity bin width. The luminosity function points obtained from the present sample are fitted using the Schechter function:

$$\Phi(L)dL = \Phi* \left(\frac{L}{L*}\right)^{\alpha} \exp\left(-\frac{L}{L*}\right) \frac{dL}{L*} \tag{0.3}$$

where α is the slope of the Schechter function at the faint end, $L*$ is the characteristic luminosity when the Schechter function transitions from exponential law at the bright end to the power law at the faint end, $\Phi*$ is the normalization factor. This luminosity function is investigated in four

redshift intervals: $2.9 < z < 6.7$, $2.9 < z < 4.0$, $4.0 < z < 5.0$ and $5.0 < z < 6.7$. Using data collected from gravitational lensing clusters has proven to be effective in studying the luminosity function at the faint end. However, such data becomes less effective at the nearby and higher characteristic luminosity values around $L*$. This problem can be addressed by including the results from previous research on the luminosity function conducted within the same redshift and luminosity range as a constraint factor for the bright end of the luminosity function. The results of the Schechter function fitting are shown in Figure 9, with gray crosses excluded from the fit due to low completeness and highly magnified sources residing in these bins.

The best-fit values of the three free parameters of the Schechter function are presented in Table 3. The slope values α of the Schechter function display a slight evolution with redshift. Within the uncertainties, the $L*$ and $\Phi*$ are consistent with the previous results. The gray crosses in Figure 9 are not included during fitting, as most of the sources in these luminosity bins have high magnifications and small completeness values. Figure 10 displays the correlation of three free parameters in the Schechter function during fitting with a 68% confidence level. The LF points in each luminosity bin and each redshift interval are presented in Table 4.

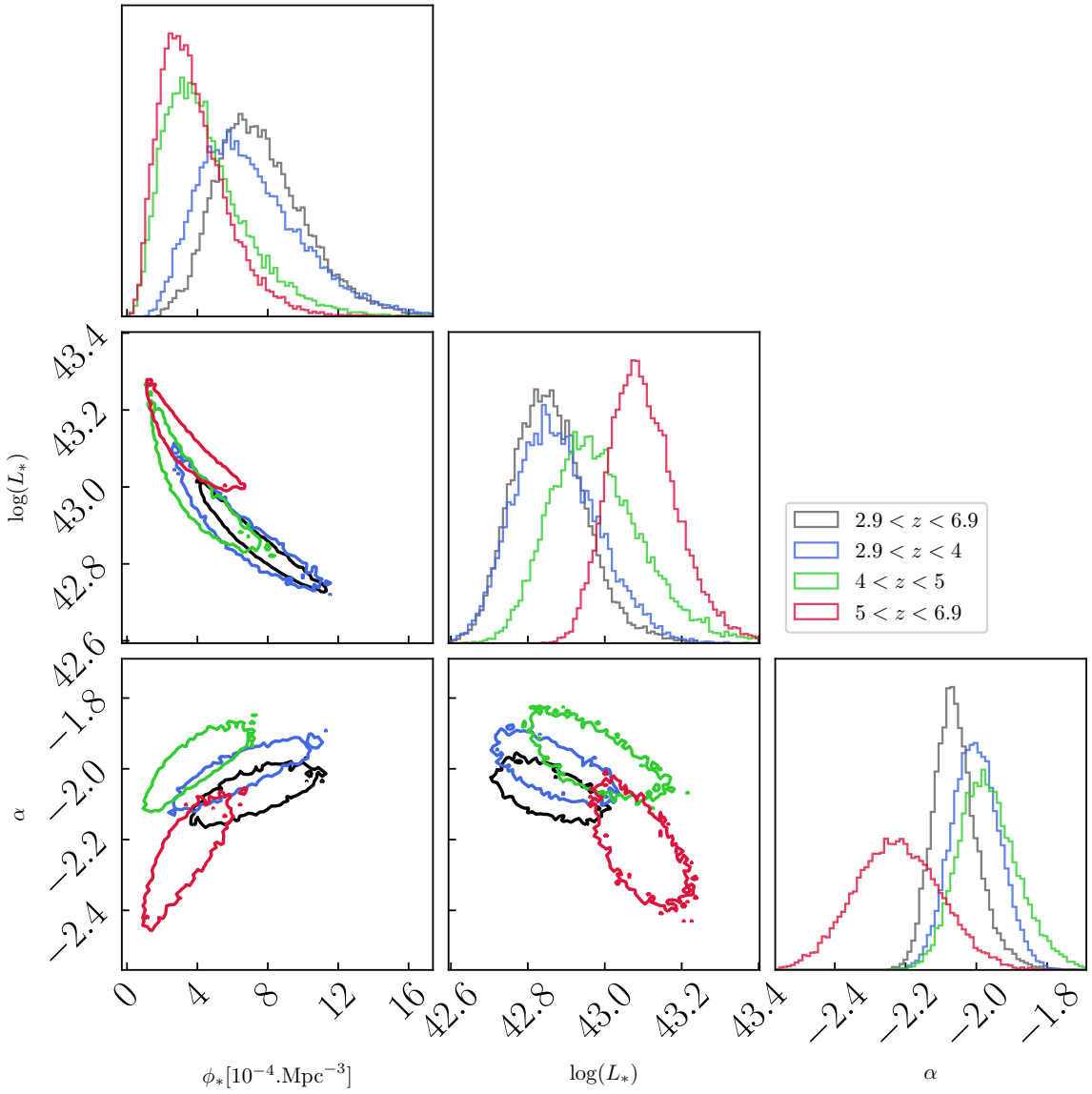

Figure 10: The correlation of three free parameters in four redshift intervals. The contour displays a confidence level of 68% during fitting.

At higher redshift intervals and fainter luminosity limits, several studies have discussed the possibility of a turnover in the shape of the luminosity function, such as Atek et al. 2018; Bouwens et al. 2022. This is presented by gray crosses in Figure 9 that were not included during fitting. To gain a better understanding of this behavior, we have introduced a modified Schechter function by adding an exponential part to represent the observed configuration:

$$\Phi(L)\exp(-L_T/L)^m = \frac{\Phi*}{L*}\left(\frac{L}{L*}\right)^{\alpha}\exp(-L/L*)\exp((-L_T/L)^m) \tag{0.4}$$

where L_T is the value where the luminosity function starts showing a turnover, it is also the value in which $d\Phi/dL = 0$, m is the curvature value orienting the shape (upward if $m < 0$ or downward if $m > 0$) of the faint part. This is presented in the lower panels of Figure 9. We found that m is about 1 while $\log L_T = 40$ and $\log L_T = 40.7$ [erg/s] with respect to the redshift range $4.0 < z < 5.0$ and $5.0 < z < 6.7$. Thanks to the lensing effect it allowed us to probe the evolution of the Luminosity Function with redshift at a fainter luminosity level compared to observations conducted in a blank

Table 4: Luminosity bins and Luminosity Function (LF) points with respect to different redshift intervals and different luminosity ranges

log (L) [erg s^{-1}]	log $(\phi)(\Delta(\log(L))=1)^{-1}$[Mpc^{-3}]	$< N >$	$< N_{corr} >$	$< V_{\max} >$ [Mpc^3]
2.9<z<6.7				
39.00<39.63<40.25	$-0.68^{+0.04}_{-0.35}$	22.4	706.0	11827
40.25<40.38<40.50	$-0.40^{+0.04}_{-0.39}$	17.6	645.4	15074
40.50<40.63<40.75	$-0.17^{+0.16}_{-0.95}$	22.8	429.3	28457
40.75<40.88<41.00	$-0.71^{+0.06}_{-0.68}$	45.2	301.5	31613
41.00<41.13<41.25	$-0.83^{+0.19}_{-0.45}$	68.9	415.7	37344
41.25<41.38<41.50	$-0.96^{+0.03}_{-0.33}$	105.0	547.9	41321
41.50<41.63<41.75	$-1.17^{+0.07}_{-0.19}$	96.4	305.5	42227
41.75<41.88<42.00	$-1.88^{+0.09}_{-0.11}$	76.4	105.1	46139
42.00<42.13<42.25	$-1.51^{+0.07}_{-0.09}$	70.4	202.5	45795
42.25<42.38<42.50	$-2.43^{+0.24}_{-0.29}$	27.5	33.5	47554
42.50<42.63<42.75	$-2.98^{+0.13}_{-0.19}$	12.9	13.0	49295
42.75<42.88<43.00	$-3.20^{+0.15}_{-0.25}$	7.7	7.8	49258
2.9<z<4.0				
39.00<39.63<40.00	$-0.15^{+0.07}_{-0.52}$	6.64	415.33	1712
40.00<40.25<40.50	$-0.10^{+0.13}_{-0.62}$	14.19	920.22	6114
40.50<40.75<41.00	$-0.85^{+0.09}_{-0.22}$	34.0	396.17	11397
41.00<41.25<41.50	$-1.08^{+0.07}_{-0.10}$	83.7	473.6	14529
41.50<41.75<42.00	$-1.01^{+0.08}_{-0.14}$	69.5	148.0	15914
42.00<42.25<42.50	$-1.53^{+0.06}_{-0.11}$	35.6	101.55	16327
42.50<42.75<43.00	$-2.93^{+0.15}_{-0.23}$	10.0	10.0	17320
4.0<z<5.0				
39.00<39.25<39.50	$-0.93^{+0.30}_{-1.91}$	1.0	38.0	730
39.50<40.00<40.0	$-1.16^{+0.11}_{-0.22}$	2.4	48.3	4904
40.0<40.25<40.5	$-0.38^{+0.09}_{-0.50}$	7.4	311.4	3159
40.5<40.75<41.00	$-0.38^{+0.11}_{-0.88}$	19.6	205.1	7662
41.00<41.25<41.50	$-1.43^{+0.10}_{-0.14}$	51.4	161.2	11044
41.50<41.75<42.00	$-1.48^{+0.1}_{-0.15}$	55.0	148.5	12164
42.00<42.25<42.50	$-2.30^{+0.13}_{-0.18}$	30.0	32.2	13182
42.50<42.75<43.00	$-3.15^{+0.20}_{-0.42}$	4.7	4.8	13433
5.0<z<6.7				
40.00<40.25<40.50	$-1.55^{+0.20}_{-0.45}$	6.0	23.8	4725
40.50<40.75<41.00	$-0.89^{+0.24}_{-1.08}$	14.3	116.5	11105
41.00<41.25<41.50	$-0.66^{+0.15}_{-0.43}$	38.9	705.5	13545
41.50<41.75<42.00	$-1.52^{+0.19}_{-0.39}$	48.2	122.9	16190
42.00<42.25<42.50	$-1.63^{+0.09}_{-0.11}$	32.3	105.2	16705
42.50<42.75<43.00	$-3.19^{+0.2}_{-0.37}$	5.9	5.9	18542

field.

Recently, two models have been developed by Garel et al. 2021; Salvador-Solé et al. 2022 to predict the Lyman Alpha Emitters Luminosity Function at redshift $z \sim 6$. It is therefore necessary to compare the results of these models to those obtained in the present work for the highest redshift range $5.0 < z < 6.7$. The first model developed by Garel et al. 2021 applies the SPHINX radiation hydrodynamics cosmological simulation to predict the Lyman Alpha LF at the EoR by estimating the radiative transfer of the sources from ISM to the IGM scales. The second model, developed by Salvador-Solé et al. 2022 uses the AMIGA model to predict the possible scenarios of single and double ionization, taking into account the impact of galaxy formation and its evolution within their feedback on the IGM. The former predicts a single hydrogen ionization stage at redshift $z \sim 6$, while the latter predicts two reionization stages at redshift $z \sim 6$ and $z \sim 10$, with two separated phases defined by a short recombination episode. The results are shown in Figure 11. At the luminosity range $41 < \log L$ [erg/s] < 42, the prediction of AMIGA double reionization is in line with the one obtained from the SPHINX simulations after correction for the IGM. In general, the LF points are in good agreement with the two predictions without any normalization requirement. At the fainter luminosity, $\log L$ [erg/s] < 41, our LF points tend to depart from Salvador-Solé et al. 2022. However, at this redshift interval, the uncertainty values are generally large, preventing us from evaluating the difference between the predictions. More observational data at the faint end of the luminosity regime and high redshift ranges are needed to solve this problem.

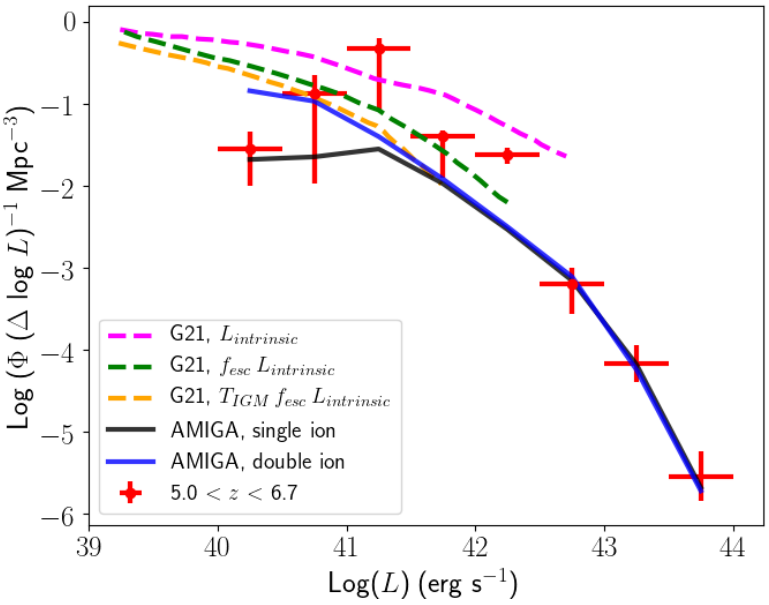

Figure 11: Comparision between the luminosity function points at the highest redshift interval $5.0 < z < 6.7$ and the AMIGA Garel et al. 2021. The pair of red crosses located in the brightest luminosity bins are average values from the literature. The blue and black solid lines are predicted from AMIGA models with respect to the single and double ionization scenarios (Salvador-Solé et al. 2022). The color dashed lines are predicted from SPHINX simulations (Garel et al. 2021) for the intrinsic luminosity value (magenta), correcting for the dust attenuation (blue) and IGM (orange).

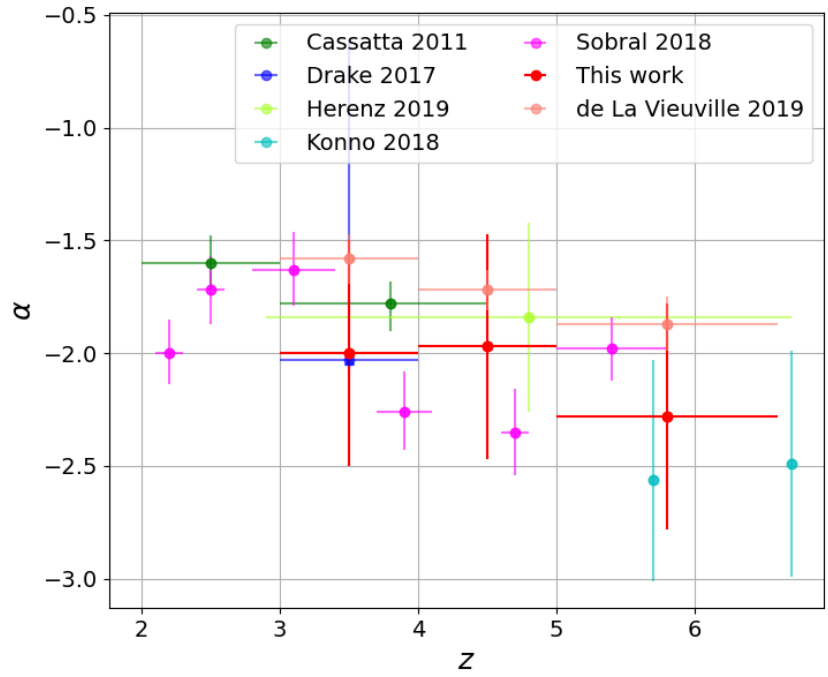

Figure 12: Evolution of the slope value with redshift. The error bars in the horizontal axis correspond to the redshift range of the survey.

In the thesis, we discuss the effects of the criterion adopted by DLV 2019 to ignore sources that have completeness values below 10% and study the evolution of luminosity function with redshift. Finally, whether sources with completeness value below 1% or 10% are removed, the turnover in shape can still be seen in the vicinity of $\log L$ [erg s^{-1}] = 41.

The thesis also presents the effect of source selection on the shape of the luminosity function versus redshift. It is worth noting that, in the present work we are using sources with a secure redshift ($zconf = 2,3$) to analyze the evolution of the luminosity function and ignore sources having a lower secure $zconf = 1$ due to low signal to noise or displaying an ambiguous line shape. For this reason, we have conducted two tests by including half of $zconf = 1$ and all the $zconf = 1$ to the present data sample. The result showed that including $zconf = 1$ in the final data sample did not significantly affect the shape of the Luminosity Function. In addition to source selection effects, we also discuss various factors contributing to systematic uncertainties in the faint end slope, including different completeness thresholds, different flux measurements, and varying fitting models. The final results are reported in Table 5.

Table 5: Faint-end slope values when applying different constraints

	z_{35}	z_{45}	z_{60}	z_{all}
Schechter fitting				
1% completeness	-2.00 ± 0.07	-1.97 ± 0.09	-2.28 ± 0.12	-2.06 ± 0.07
10% completeness	-1.78 ± 0.06	-1.83 ± 0.12	-1.75 ± 0.10	-1.46 ± 0.05
1% completeness and using the flux values obtained from source extractor	-2.10 ± 0.06	-1.97 ± 0.08	-2.24 ± 0.11	-1.82 ± 0.03
1% completeness and including all the $zconf = 1$ source	-1.83 ± 0.17	-1.92 ± 0.09	-1.94 ± 0.10	-2.29 ± 0.09
Linear fit				
1% completeness	-1.76 ± 0.27	-1.99 ± 0.17	-1.96 ± 0.54	-2.12 ± 0.16
10% completeness	-1.55 ± 0.17	-1.63 ± 0.21	-1.66 ± 0.24	-1.64 ± 0.12
Final slope value	-2.00 ± 0.50	-1.97 ± 0.50	-2.28 ± 0.50	-2.06 ± 0.60

Based on the obtained results on the luminosity function, Chapter 5 focuses on luminosity density and the conversion of this parameter into star formation rate density by integrating the luminosity function with respect to luminosity. While the shape of the luminosity function at the bright end remains unaffected by the completeness threshold value and source selection and is entirely consistent with the previous studies conducted in the blank fields, the faintest part is constrained by both these mentioned factors. For this reason, the result of the integration is not significantly influenced by the upper limitation, whereas the lower limitation is certainly an impacting factor. I applied two lower limitation values: one is log L [erg s^{-1}] = 39.5 to cover all the data samples, and the other is log L [erg s^{-1}] = 41 to include only the most secure determinations of the LF. These results, when compared to the critical value for the star formation density (i.e., the amount required to reionize the Universe at a given redshift), suggest that galaxies selected by their Lyα emission could be responsible for reionization assuming a Lyα photon escape fraction of 8%, with a typical clumping factor of ~ 3. In any case, they appear to play a substantial role in the reionization process.

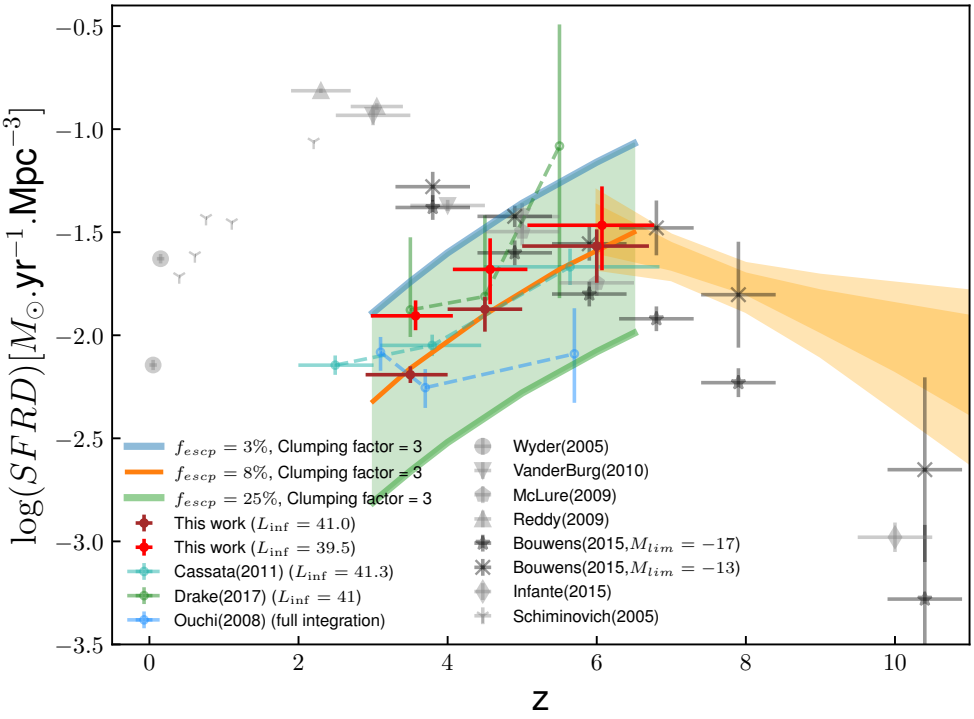

Figure 13: Evolution of star formation rate density with redshift. The red and brown-reddish crosses represent the results obtained when applying lower integration limits of log L [erg s^{-1}] = 39.5 and log L [erg s^{-1}] = 41.0, respectively. The blue, orange, and green solid lines indicate the critical values obtained with escape fraction values of 3%, 8% và 25%, combined with a typical clumping factor of 3.

Chapter 6 presents a general discussion of the final results and future prospects. Subsequently, I hope to continue this work on the Luminosity Function of Lyman alpha emitters using data collected behind 25 lens clusters belonging to the MUSE GTO program, or already available on the ESO archives. I also worked during my thesis on the construction of the catalogs for the fields on which I worked, by determining the redshifts of all the background galaxies from signatures other than Lyα, such as the lines of Balmer's series or OII-3727 at lower redshift. I also plan to work on JWST data and Euclid in a higher redshift range for Lyman alpha emitters. The determination

of the Luminosity function remains fundamental to study the global evolution of ionizing sources according to the redshift. The excellent combination between JWST and MUSE also offers the possibility to analyze the production of ionizing photons with high efficiency.

CONCLUSIONS

The thesis presents a study of the contribution of star forming galaxies to the cosmic reionization via studying the Luminosity function of Lyman alpha emitters in a redshift range of $2.9 < z < 6.7$ behind 17 lensing clusters observed by MUSE/VLT.

We selected 600 lensed LAEs that covered four orders of magnitude in magnification corrected Lyman alpha luminosity $39 < \log L[\mathrm{erg/s}] < 43$. In comparison with the previous data sample conducted by DLV 2019, the present data shows significant abundance (four times more) and contains more faint sources at $\log L < 41.0$ [erg/s]. The contribution of these sources to cosmic reionization has been estimated by using the $V_{\max}$ method as the one presented in DLV 2019 with some improvements that have been introduced. The main results of the thesis have been listed and discussed as follows:

- The correlation between the magnification of cosmic co-moving volume of individual sources has been discussed. For the highly magnified sources, this correlation is shown by an exponential function when the magnification value of the sources was varied randomly within $2 - sigma$. We can use a linear function to show the correlation for the modest magnification sources.

- The evolution of the Luminosity Function with redshift has been investigated in four redshift intervals $2.9 < z < 4.0$, $4.0 < z < 5.0$, $5.0 < z < 6.7$ and $2.9 < z < 6.7$. The total co-moving volume of the survey is about $\sim 50000\ Mpc^3$, three times larger than the one found in DLV 2019. However, this value is smaller than the ones used for data observed in the blank field. The explanation for this difference is a constraint of the magnification values caused by the lensing effect. The sources behind A2744 are still significant contributors to the total co-moving volume.

- The best fit values of the Schechter function in redshift interval $2.9 < z < 6.7$ are $\alpha = -2.06^{+0.07}_{-0.05}$, $\Phi*[10^{-4}\ \mathrm{Mpc}^3] = 7.41^{+2.70}_{-2.20}$, $\log L[\mathrm{erg/s}] = 42.85^{+0.10}_{-0.10}$.

- When $\log L[\mathrm{erg/s}] > 42$, our LF points are consistent with literature using data observed in blank fields and lensing fields.

- The contribution of the sources to the faint luminosity bins has been determined. Most of them are highly magnified sources. The source density in this region was estimated via the slope value of the Schechter function $\alpha \sim -2$. The slope values obtained from Schechter fitting and a linear fitting are consistent with the uncertainties. The slope values in four redshift intervals are in line with the literature, i.e., Drake et al. 2017 and 20% higher than the ones obtained by DLV 2019. This value also is in line with Herenz et al. 2019 in an interval redshift of $2.9 < z < 6.7$. The thesis also accounted for the effects of source selection, different completeness thresholds, the final slope values are -2.0 ± 0.50, -1.97 ± 0.50, -2.28 ± 0.50 and -2.06 ± 0.60 in redshift interval $2.9 < z < 4.0$, $4.0 < z < 5.0$, $5.0 < z < 6.7$ and $2.9 < z < 6.7$, respectively.

- The direct comparison to the results obtained by DLV 2019, the slope values of the Schechter function show evolution with redshift, however the uncertainty in each redshift interval is still large. We found a turnover in the shape of the Luminosity Function at the two highest redshift intervals, $4.0 < z < 5.0$ and $5.0 < z < 6.7$ when $\log L$ [erg/s] < 41. This is explained by the decrease of cold gas in the dark matter halos which are low massive (Jaacks et al. 2013; Yue et al. 2016).

- The results obtained from studying the evolution of the Luminosity Function with redshift have been used to estimate the contribution of star forming galaxies to the cosmic re-ionization. The turnover in shape of the Luminosity Function when $\log L$ [erg/s]< 41 is the reason for the significant increase of the SFRD at redshift $z = 3.0 - 6.0$. This confirms the large contribution of LAEs to the cosmic reionization.

- The contribution of LAEs is significant in maintaining the ionized state of Hydrogen atoms in the Universe. At redshift $z \sim 6$, its contribution is comparable to the LBGs.

As mentioned above, uncertainties of measurements in the thesis are still large when estimating contribution of Lyman alpha emitters to the cosmic re-ionization. Using data observed from different telescopes and different redshifts can help to improve the results obtained from the thesis.

THE NEW CONTRIBUTION OF THE THESIS

This is the largest data sample of Lyman Alpha Emitters observed by lensing using the MUSE/VLT. Thanks to gravitational lensing effect allowed us to observe the signal of sources having $\log L$ [erg/s] < 41, the threshold could not reached by observations in blank field. Therefore, the data and the present results provide crucial information for understanding in this research domain.

LIST OF PUBLICATIONS

1. T. T. Thai, P. Tuan-Anh, R. Pello, I. Goovaerts, J. Richard, A. Claeyssens, G. Mahler , D. Lagattuta, G. de la Vieuville, E. Salvador-Solé, T. Garel, F. E. Bauer, A. Jeanneau , B. Clément, and J. Matthee. Probing the faint-end luminosity function of Lyman-alpha emitters at $3 < z < 7$ behind 17 MUSE lensing clusters. AA, 2023, 678, A139.

2. Ilias Goovaerts, Roser Pello, Tran Thi Thai, Pham Tuan-Anh, Johan Richard, Adélaïde Claeyssens, Emile Carinos, Geoffroy de la Vieuville, Jorryt Matthee. Evolution of the Lyman-α emitting fraction and UV properties of lensed star-forming galaxies between $2.9 < z < 6.7$. AA, 2023, 678, A174.

3. T. T. Thai, P. Tuan-Anh, R. Pello, I. Goovaerts. Studying the luminosity function of lyman alpha emitters selected behind 17 lensing clusters from multi-unit spectroscopic explorer (muse/vlt) observations. Proceeding in 16th OMEG conference.